Journal of Metals, Materials and Minerals, 34(4), 2092, 2024

Impact of hot rolling, Zn and Sn on the mechanical and corrosion characteristics of Mg-Zn-Ca alloys

Halil EREN[1,2], Ali GÜNGÖR[1,*], Erkan KOÇ[3], and Harun ÇUĞ[4]

[1] *Metallurgical and Materials Engineering, Karabuk University, 78050 Karabuk, Turkey*
[2] *Material and Material Processing Technologies Department, Cankiri Karatekin University, 18100 Cankiri, Turkey*
[3] *Biomedical Engineering, Karabuk University, 78050 Karabuk, Turkey*
[4] *Mechanical Engineering, Karabuk University, 78050 Karabuk, Turkey*

***Corresponding author e-mail**: agungor@karabuk.edu.tr

Received date:
23 June 2023
Revised date:
7 October 2024
Accepted date:
7 November 2024

Keywords:
Magnesium alloys;
Corrosion;
Material science;
Biodegradable materials;
Hot rolling

Abstract

In this study, it was aimed to develop a biodegradable metallic plate that is an alternative to bioinert metal plates. The main advantage of using biodegradable materials for implants is that they can be gradually replaced with the patient's own tissue, which reduces the need for additional surgeries to remove the implant after it has served its purpose. Magnesium and its alloys can provide biocompatibility as orthopedic implant materials. Mg-Zn-Ca and Mg-Zn-Ca-Sn alloys were prepared using the gravity die casting method. Zn (1.0 wt% and 2.0 wt%) and Sn (0.0 wt%, 0.5 wt% and 1.0 wt%) ratios were used as variables, and the Ca ratio (0.3 wt%) was kept constant in all alloys. After homogenization heat treatment, alloys were hot rolled. Hot rolling resulted in grain refinement, much higher yield and tensile strength, and hardness at the expense of the lower strain. However, hot rolling had a detrimental impact on the corrosion resistance of the alloys. Among the alloys, ZX20-h alloy showed the highest yield and tensile strength before and after corrosion tests. The lowest corrosion rate was measured in ZXT200 alloy as 5.1 mm·year^{-1} after 10 day of immersion. Although ZX20-h alloy has a higher corrosion rate (13.56 mm·year^{-1}) than ZXT200 alloy, it can be improved further to be used as biodegradable bone support plate material.

1. Introduction

Every year, people encounter bone fractures as a result of accidents and injuries. Therefore, the need for implant materials for the treatment of these fractures increases continuously. It is required that implant materials must be highly biocompatible with the surrounding tissue and have nontoxic properties. Metallic implant materials are especially preferred because of their superior strength, ductility, and toughness. According to the corrosion resistance of the alloys, biomaterials are grouped as permanent and degradable implant materials [1,2]. Permanent metal implants, chemically stable, can cause physical irritation and inflammation as long as they remain fixed in the human body. They also adversely affect human health, and after the healing of the bone structure, they are removed with another surgery within 1 year to 2 year [3,4]. Each surgery can cause pain, medical risks, and extra costs for the patient [2-5]. In addition, the implant materials used today reduce the tensile strength of the bone, lead to bone loss, and may also cause the bone fracture again in some cases [6,7]. On the other hand, the chemical stability of degradable biomaterials in contact with the body fluid is low, and degradation occurs with time. To develop degradable biomaterials is a complex process due to the combined evaluation of engineering and medical requirements [8,9]. Biodegradable materials to be developed as implants must maintain their mechanical strength during the healing process of the tissue and should be degraded and excreted from the body after the tissue has healed. For example, the time for a bone to heal completely varies depending on the extent of the damage and the type of bone, and it generally takes between 12 week and 52 week [9]. Therefore, it is expected that a biodegradable material is to be able to maintain its mechanical properties for at least 12 week and then to have a controlled degradation.

Biodegradable implant materials provide significant advantages because they can provide good mechanical properties and remove the additional surgeries after healing [2,10,11]. Among the implant materials, Mg-based alloys are becoming increasingly popular as biodegradable materials [1]. Although magnesium alloys offer superior mechanical characteristics and biocompatibility than degradable ceramic and polymer biomaterials, their low corrosion resistance is a limiting factor [1,2]. Therefore, the corrosion resistance and mechanical properties of magnesium alloys should be improved by alloying elements, the application of thermomechanical processes, and heat treatments to control the microstructure to be able to obtain the desired chemical, physical, and mechanical properties. Alloying is one of the most commonly used techniques to alter the material's properties. In Mg-based biomaterials, biocompatible alloying elements such as Zn, Ca, Sn, etc. are preferred due to their abundance in the human physiological system, nutrition, and non-toxic properties [12,13]. In recent years,

Mg alloys have come to the fore as biodegradable metal implant materials, and numerous studies have been done on Mg alloys [14-16].

Zhao *et al.* studied the microstructure and corrosion behavior of biodegradable Mg-Sn implant alloys. They observed that the Mg_2Sn secondary phase increased in the structure by increasing Sn ratio. They determined that the corrosion resistance of Mg-Sn alloys decreased with increasing Sn content. They revealed that Mg-1Sn alloys are safe as biodegradable implant alloys [17]. Jhamb *et al.* similarly studied the corrosion properties of Mg-xSn (x = 0, 1, 2, and 3 wt%) alloys. They observed that the increase in the Sn ratio caused a decrease in corrosion resistance. In studies on Mg-1Zn alloys, it is seen that Sn addition largely reduces the degradation rate by converting pitting corrosion into a uniform corrosion mode, but excessive Sn addition (above 1.5 wt%) conversely worsens the degradation performance due to the formation of coarse Mg_2Sn phases [18,19]. Weiyan *et al.* studied the Mg-4Zn alloy. They found that the addition of small amounts of Sn (1 wt% and 1.5 wt%) slightly improved the mechanical properties and significantly controlled the bio-corrosion rates. However, they observed that as the Sn content increased above 1.5 wt%, the corrosion performance deteriorated as a result of the increased formation of Mg_2Sn phases [20]. El-Mahallawy *et al.* studied Mg-xSn-0.04Mn alloys (x = 0.25 wt% and 1.53 wt%). They were prepared by casting, heat treatment, hot extrusion, and hot rolling. After thermomechanical treatment, they obtained a significant increase in strength and ductility and a decrease in corrosion rate [21]. In Mg-Ca-Zn alloys, the Zn/Ca atomic ratio affects corrosion resistance by forming eutectic (α-Mg+$Ca_2Mg_6Zn_3$) and divorced-eutectic structures (α-Mg+Mg_2Ca+$Ca_2Mg_6Zn_3$) [22]. Wahid *et al.* studied the effect of Sn on Mg-3Zn-0.3Ca-xSn (x = 1.5, 3, and 5 wt%) alloy. They noted that when the Sn ratio increased from 1.5% to 5%, the CaMgSn phase became thinner and changed from rod-like to needle-like or hair-like. They observed that Ca and Sn preferentially form the CaMgSn ternary phase instead of Mg_2Ca or the $Ca_2Mg_6Zn_3$ phase. It was observed that the Mg_2Sn phase was formed in the structure as the Sn ratio increased from 1.5% to 3% [23]. Rout *et al.* showed that alloys containing more than 1 wt% Ca have very low corrosion resistance and can not be used as implant materials [24]. Zn, as another alloying element, forms a protective film on the surface of the alloy, and prevent further corrosion. In addition, Zn improves the strength of the Mg by precipitation hardening due to the high solubility of Zn in magnesium. However, in order to obtain a good combination of mechanical properties and corrosion resistance, the Zn content should be limited (less than 2.0 wt%) [25-27]. The Sn element improves the corrosion resistance of the Mg by improving the electrode potential of the Mg matrix. Previous studies showed that the Sn content up to 1 wt% exhibited good in vitro biocompatibility [19,28]. Studies examining the effects of low and high Ca content (0.3 wt% and 1.8 wt%) on designed alloys have shown that alloys containing low Ca content (0.3 wt%) have more positive results in both mechanical properties and corrosion performance [29].

Although numerous studies have been carried out to improve the mechanical and corrosion properties of Mg-based alloys, the influence of the alloying elements, heat treatment, and thermomechanical process on the material properties of Mg alloys have not been clear yet. In this study, the effects of Zn and Sn elements and hot rolling on the mechanical and corrosion behaviour of Mg-Ca-Zn alloys were investigated. Our study focuses on the corrosion resistance and mechanical properties of the alloys not only before and after hot rolling but also after immersion corrosion to assess the mechanical integrity of the alloys.

2. Materials and methods

Alloys were produced using high-purity Mg ingots (99.9%), Mg-20Sn, Mg-25Ca, and Mg-30Zn master alloys, and casting was carried out under protective gas in a closed system consisting of two parts. The melting zone is the upper part of the furnace, and the casting zone is the lower part of the furnace. A stainless steel crucible was used in the melting zone. The inner diameter of the crucible is 150 mm, and its depth is 250 mm. Atmosphere control was provided with Argon gas in the melting zone, while a 0.8% SF6 + CO_2 gas mixture was used in the casting zone. After 20 min duration at 800°C, liquid metal was allowed to run and fill the mould. After casting, homogenization of the alloys was performed at 400°C for 12 h.

The Rigaku Primus II - X-ray fluorescence spectrometer and the Rigaku Ultima IV X-ray diffractometer were utilized to do phase analysis. 2 Theta-Theta measurements were conducted between 10° and 90° at a scan rate of $0.02°{\cdot}s^{-1}$ using 30 keV·20 mA^{-1}.

Cast alloys were sliced with wire erosion in the form of plates after homogenization heat treatment. The dimensions of the plates were 4.5 mm × 20 mm × 180 mm in thickness, width, and length, respectively. These plates were used for hot rolling, tensile testing, microstructure analysis, hardness measurements, and corrosion tests.

The hot rolling was performed on twin rollers at a speed of 20 rpm. Two samples from each alloy were hot rolled. Samples with 4.5 mm in thickness were subjected to 10% deformation in each pass of hot rolling, for a total of 40% deformation. All samples were heated to 400°C and held there for 30 min before the first pass. In between the passes, the samples were held at 400°C for 15 min before the subsequent pass.

The Vickers hardness (HV) of the alloys before and after hot rolling was measured using a Q10 A+ QNESS microhardness tester. During the hardness measurement, a load of 0.5 kg was applied for 15 s. Tensile tests were conducted at a tensile speed of 2 $mm{\cdot}min^{-1}$ using the Zwick/Roell Z600 Universal Testing Machine. Microstructure analysis of all alloys was performed using Carl Zeiss ULTRA PLUS FESEM. Before Scanning Electron Microscope (SEM) characterizations, the etching process was carried out in acetic picral (6 g picric acid + 5 mL acetic acid + 10 mL distilled water + 100 mL ethyl alcohol) and nital (4 mL nitric acid + 100 mL ethyl alcohol), respectively [30].

Immersion corrosion tests were done in a Memmert brand ETUV furnace. The volume 30 mL of Diagnovum Hank's Balanced Salt Solution (BSS) was determined for each sample according to ASTM Standard G31-72 [19]. The samples were cleaned using purified water and ethanol for 5 min in an ultrasonic cleaner before corrosion tests. After corrosion tests, all samples were washed using purified water, ethanol, and chromic acid for 5 min, respectively. The initial and final weights of the samples were measured using a precision balance with 1/10000 sensitivity. Corrosion tests were conducted by immersing the samples in corrosive medium at a temperature of 37 ± 1°C for 1 day, 5 day, and 10 day.

3. Results and discussions

3.1 X-ray fluorescence (XRF) analysis results

The results of the X-ray fluorescence (XRF) analyses are given in Table 1. It shows that the nominal composition of the alloys was approximately achieved.

3.2 X-ray diffraction (XRD) results

The X-ray diffraction (XRD) patterns of the alloys are given in Figure 1. It is seen that strong signals from the α-Mg crystals and weak signals from the intermetallic phases were obtained. Weak XRD peaks of the secondary phases are due to the lower volume fraction and smaller size of the intermetallic phases. In addition, XRD analysis showed that the $Ca_2Mg_6Zn_3$ intermetallic phase formed in the ZX10 and ZX20 alloys. On the other hand, it was observed that CaMgSn and Mg_2Sn phases formed in Sn containing alloys. The secondary phases observed in these alloys are consistent with the literature results. Zhang *et al.* studied the mechanical, microstructure, and corrosion resistance of Mg-Zn-Mn-Ca alloys, and they determined that primary α-Mg and divorced eutectic phases (α-Mg+Mg_2Ca+$Ca_2Mg_6Zn_3$) form when Zn/Ca atom ratio is less than 1.0 to 1.2, while α-Mg and eutectic phases (α-Mg+$Ca_2Mg_6Zn_3$) form when Zn/Ca atom ratio is higher than 1.0 to 1.2 [22]. Since Zn/Ca atom ratio of the alloys studied here is higher than 1.0 to 1.2, the Mg_2Ca phase is not expected to form. As expected, the Mg_2Ca containing divorced eutectic structure was not determined in the XRD patterns of the alloys. According to the Hume Rothery rules, intermetallic phases form instead of solid solutions in systems in which the electronegativity difference between the components is large. Zhao *et al.* observed that the Mg_2Sn phase formed in Mg-Ca-Zn-0.5/1 Sn alloys because of a large electronegativity difference between Mg and Sn [18].

3.3 Scanning electron microscopy - Energy dispersive X-ray spectroscopy (SEM-EDX) analysis results

Scanning electron microscope images of the alloys before hot rolling are shown in Figure 2. As it is observed from Figure 2(a) and Figure 2(d), the Sn free alloys (ZX10 and ZX20) have relatively larger equiaxed grains and a lower volume fraction of the secondary phases than those of Sn containing alloys. The large grain size of the alloys is attributed to the homogenization heat treatment done at 400°C for 12 h. Thermal energy obtained during homogenization heat treatment provides driving force for grain boundary migration, and as a result, grain growth occurs. In addition, the $Ca_2Mg_6Zn_3$ phase observed in Sn free alloys in X-ray diffraction (XRD) analyses was observed along the grain boundaries and inside the grains. Increasing the Zn ratio from 1.0 wt% to 2.0 wt% of Sn free alloy results in a higher volume fraction of the secondary phase and a slightly lower grain size. The reduction in grain size with increasing Zn content can be explained with the high growth restriction factor of Zn [31]. Since solubility of Zn and Ca decreases with decreasing temperature, front of the solid-liquid interface is enriched with these elements that results in constitutional undercooling and fine grains formation. The microstructures of ZX10 and ZX20 alloys consist of the α-Mg matrix and the α-Mg+$Ca_2Mg_6Zn_3$ eutectic phases. The eutectic phase in the grains has a granular shape, while it has a lamellar shape along the grain boundaries.

New intermetallic phases, CaMgSn and Mg_2Sn, form with the addition of Sn to the Mg-Zn-Ca system. The modification of ZX10 alloy with 0.5 wt% Sn (ZXT100, Figure 2(b)) results in a higher volume fraction of secondary phases, a finer grain size, and the formation of CaMgSn and Mg_2Sn intermetallic phases. The increase in volume fraction of secondary phases is due to the formation of Sn containing intermetallic phases (CaMgSn and Mg_2Sn). Increasing the Sn ratio of the alloy to 1.0 wt% (ZXT101 alloy, Figure 2(c)) results in a much higher volume fraction of secondary phases and a much finer grain size. The reduction in grain size with an increasing volume fraction of secondary phases implies that migration of grain boundaries is restricted due to the pinning effect of fine CaMgSn and Mg_2Sn particles. It is observed that the shape, size, and distribution of the secondary phases are similar in both ZXT100 and ZXT101. However, the comparison of micro images in Figure 2(b) and Figure 2(e) shows that ZX100 has more uniformly distributed finer secondary phases than ZX101. Similarly, modification of ZX20 alloy with 0.5 wt% Sn (ZX200) results in a higher volume fraction of intermetallic phases and a lower grain size (Figure 2(f)). The increase in volume fraction of the $Ca_2Mg_6Zn_3$

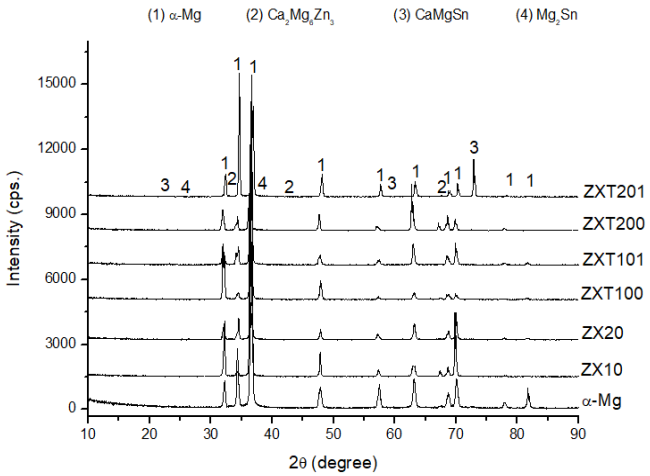

Figure 1. X-ray diffraction (XRD) results of alloys (α-Mg: Pure Magnesium).

Table 1. X-ray fluorescence (XRF) results of the alloys after the homogenization heat treatment (wt.%) (Z: Zn, X: Ca, T: Sn).

Designation	Mg	Zn	Ca	Sn	Others
ZX10	98.71	0.96	0.25	-	0.08
ZX20	97.69	2.00	0.26	-	0.06
ZXT100	98.10	0.97	0.26	0.56	0.10
ZXT101	97.69	0.88	0.26	1.08	0.09
ZXT200	97.25	1.95	0.26	0.54	0
ZXT201	96.48	2.00	0.29	1.24	0

intermetallic phase in the ZX20 alloy is attributed to the higher Zn ratio of the alloy. Increasing the Sn ratio of the ZX20 alloy to 1.0 wt.% (ZX201), the volume fraction of the secondary phases increases further, and grain size continues to decrease. The presence of higher Zn and Sn elements in the system increases the formation of secondary phases formation. In addition, segregation of Zn and Ca atoms in Mg-Zn-Ca systems to the front of the liquid-solid interface during solidification causes constitutional undercooling that restricts grain growth [32]. As a result, both Zn and Sn influence the grain size, type, and volume fraction of intermetallic phases. If the micro images of the alloys given in Figure 2 are compared, it is seen that Zn is more effective at refining the grain size of the alloy than Sn.

The microstructures of the hot rolled alloys are presented in Figure 3. It is seen that hot rolled ZX10 and ZX20 alloys (Figure 3(a) and Figure 3(d)) have finer secondary particles distributed along the grain boundaries and inside the grains as well as fine grain size than the unrolled ZX10 and ZX20 alloys. The fine secondary phases can be attributed to the stress-induced precipitation during hot rolling. In addition, cracks are observed on the coarse secondary phases that are distributed along the grain boundaries (Figure 3(b-c,e-f). Fracturing of intermetallic phases during plastic deformation is due to their low toughness, which is commonly observed in brittle materials. Moreover, the presence of very fine grains in hot rolled alloys in the absence of post heat treatment indicates that dynamic recrystallization occurred during hot rolling.

Energy dispersive X-ray spectroscopy (EDX) analyses were used to determine the composition of the secondary phases present in the alloys. In EDX analyses, small fields rather than a point were used to measure the compositions to increase the yield of X-ray photons. As a representative result, the EDX analyses performed on the ZX20 and ZXT201 alloys are shown in Figure 4.

The EDX analysis of ZX20 alloy in Figure 4(a) and Table 2(a) shows that the microstructure of ZX20 alloy consists of α-Mg matrix (number 1), eutectic constituent of $Ca_2Mg_6Zn_3$ phase (number 2 and 4), and Mg_2Ca phase (number 3). However, it should be noted that the Mg_2Ca phase was not detected by XRD. When Figure 4(b) and Table 2(b) are examined, it is seen that α-Mg (point 1), Mg_2Sn, and CaMgSn phases form with Sn addition. The lamellar Mg_2Sn phase in the eutectic α-Mg+Mg_2Sn structure (number 3) is observed at the grain boundaries. The presence of Zn at these points indicates the possible formation of a Mg-Zn compound. Similarly, the CaMgSn phases (number 2) were observed in granular forms in the grains.

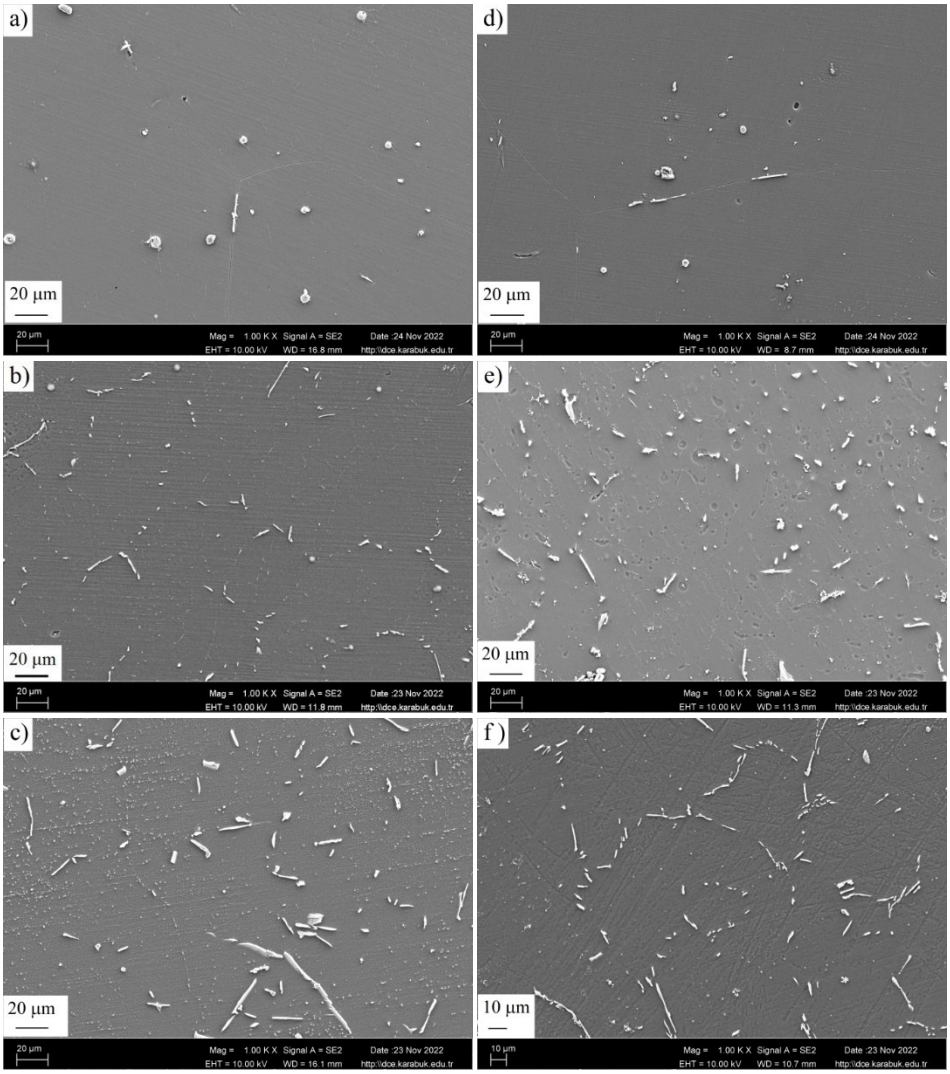

Figure 2. Scanning Electron Microscopy (SEM) images of (a) ZX10, (b) ZXT100, (c) ZXT101, (d) ZX20, (e) ZXT200, and (f) ZXT201 before hot rolling.

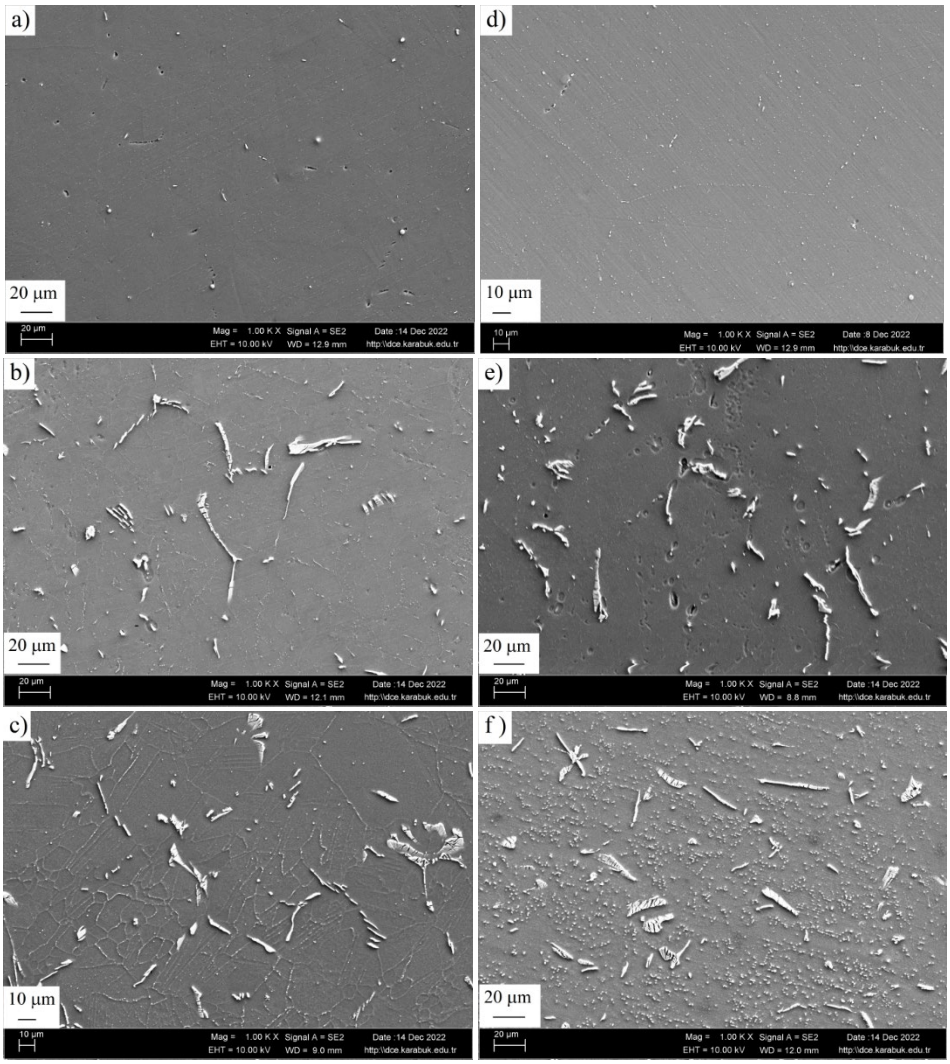

Figure 3. Scanning Electron Microscopy (SEM) images of (a) ZX10-h, (b) ZXT100-h, (c) ZXT101-h, (d) ZX20-h, (e) ZXT200-h, and (f) ZXT201-h after hot rolling (h: Hot rolled).

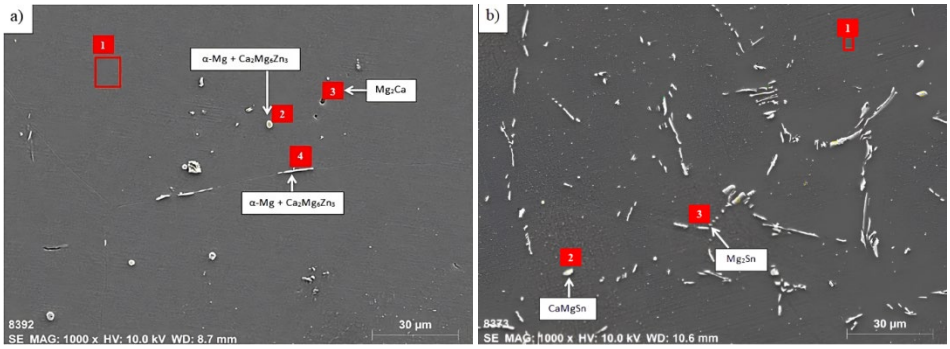

Figure 4. EDX analysis results: (a) for ZX20 alloy, and (b) for ZXT201 alloy.

Table 2. Atomic percentages (%) obtained by EDX analysis of the points indicated in Figure 4(a) for ZX20 alloy and Figure 4(b) for ZXT201 alloy).

Figure 4(a) Point	**Mg (at%)**	**Ca (at%)**	**Zn (at%)**	**Figure 4(b) Point**	**Mg (at%)**	**Ca (at%)**	**Zn (at%)**	**Sn (at%)**
1	98.34	0.00	1.66	1	98.32	0.00	1.58	0.10
2	63.49	12.40	24.11	2	78.85	3.20	8.38	9.57
3	71.09	27.18	1.73	3	74.23	0.00	12.34	13.43
4	67.77	10.04	22.19					

3.4 Hardness results

The Vickers hardness (HV0.5) of the alloys before and after hot rolling was measured. For each sample, four measurements were conducted, and the average hardness of the alloys was obtained. The hardness of the alloys is given in Figure 5.

The application of hot rolling enhanced the hardness of the alloys. The average hardness of the alloys demonstrates that there is a parallel correlation between the hardness and the zinc ratio of the alloy. However, it is found that Sn has a negative effect on hardness due to the fact that Sn containing alloys show lower hardness. Therefore, it can be said that Sn has a softening effect on the hardness of the alloys because Sn free alloys have higher hardness values than Sn containing alloys. Among the alloys, the highest hardness value of 60.3 (± 0.2 HV) was seen in the hot rolled ZX20-h alloy, which does not contain Sn and has a high Zn content.

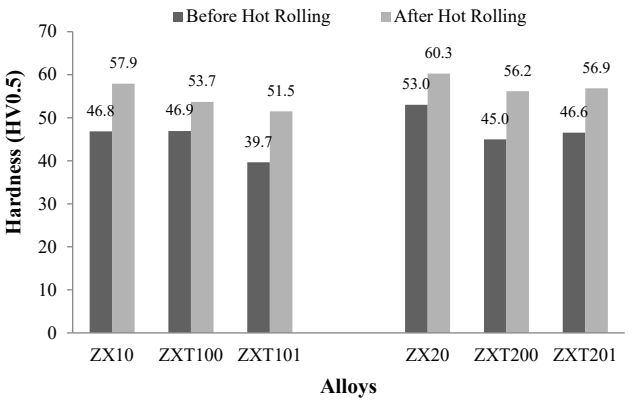

Figure 5. Vickers hardness (HV) of alloys before and after hot rolling.

3.5 Tensile test results

Mechanical properties and stress-strain curves of the Mg-Zn-Ca alloys without Sn addition were given in Table 3 and Figure 6. The large amount of plastic strain observed in stress-strain curves indicates that ductile fracture occurred in the alloys. However, hot rolling results in much lower strain at fracture but higher yield and tensile strengths. This indicates that grain refinement, which occurs during the dynamic recrystallization (DRX) process during hot rolling, improves the strength of the alloy according to the Hall-Petch relation at the expense of ductility. In addition, the dispersion of fine secondary particles in the matrix due to the hot rolling process is another strengthening factor. The contribution of fine particles to the strength of the alloy occurs through the Zenner pining mechanism. It is seen that the increase in yield strength of ZX10 alloy after hot rolling is about 220%, and it is about 250% for ZX20 alloy after hot rolling. Similarly, the increase in tensile strengths of the hot rolled ZX10 and ZX20 alloys is about 70% and 84%, respectively. On the other hand, fracture strain of ZX10 alloy decreases about 30% after hot rolling while fracture strain of ZX20 alloy increases about 20% after hot rolling. The increase in strain at fracture for the ZX20 alloy can be attributed to the finer grain size of ZX20 alloy. When the Zn content of the alloy is taken into consideration, it is seen that increasing the Zn ratio of the alloy increases the strength of the alloy before and after hot rolling but reduces the ductility of the alloy before hot rolling. The contribution of the Zn element to the strength of the alloy occurs through the solid solution strengthening mechanism, precipitation hardening, and grain refinement mechanisms as discussed above.

Mechanical properties and stress-strain curves of the alloys containing Sn were given in Table 4 and Figure 7 and Figure 8.

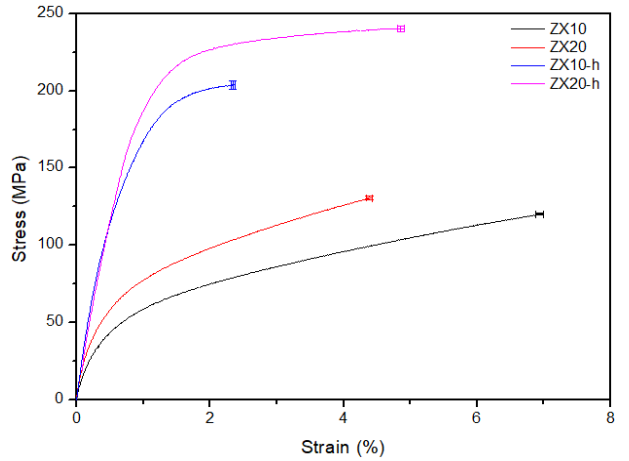

Figure 6. Stress-Strain curve of Mg-Zn-Ca alloys without Sn addition (h: Hot rolled).

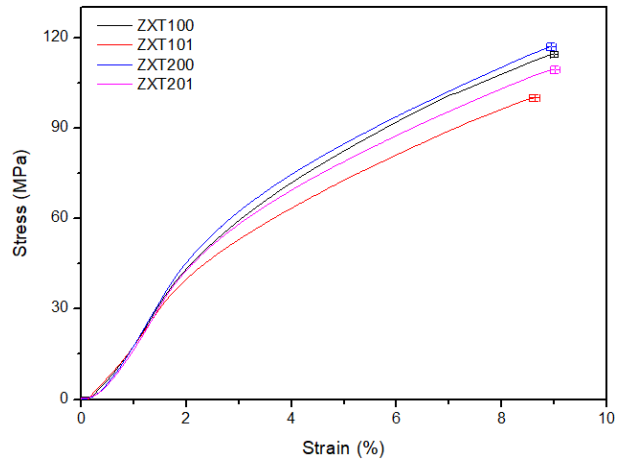

Figure 7. Stress-Strain curve of Sn added alloys before hot rolling.

Table 3. Tensile properties of Mg-Zn-Ca alloys without Sn addition (h: Hot rolled).

Alloys	Yield strength (σ_y) (MPa)	Tensile strength (σ) (MPa)	Strain (ε) (mm.mm^{-1})
ZX10	40.50	120.07 ± 0.75	6.94 ± 0.06
ZX20	50.38	130.70 ± 1.08	4.39 ± 0.05
ZX10-h	130.61	203.90 ± 2.88	2.55 ± 0.04
ZX20-h	177.44	240.50 ± 1.85	5.28 ± 0.05

Table 4. Tensile properties of Sn added alloys (h: Hot rolled).

Alloys	Yield strength (σ_y) (MPa)	Tensile strength (σ) (MPa)	Strain (ε) ($mm.mm^{-1}$)
ZXT100	51.43	114.53 ± 0.95	9.39 ± 0.07
ZXT101	44.25	99.94 ± 1.15	8.82 ± 0.09
ZXT200	53.82	116.91 ± 1.37	9.32 ± 0.10
ZXT201	49.45	109.33 ± 1.28	9.47 ± 0.10
ZXT100-h	97.87	173.90 ± 2.17	2.88 ± 0.04
ZXT101-h	89.40	158.10 ± 2.20	2.60 ± 0.04
ZXT200-h	115.98	204.08 ± 2.50	3.06 ± 0.04
ZXT201-h	114.13	187.20 ± 2.26	2.98 ± 0.04

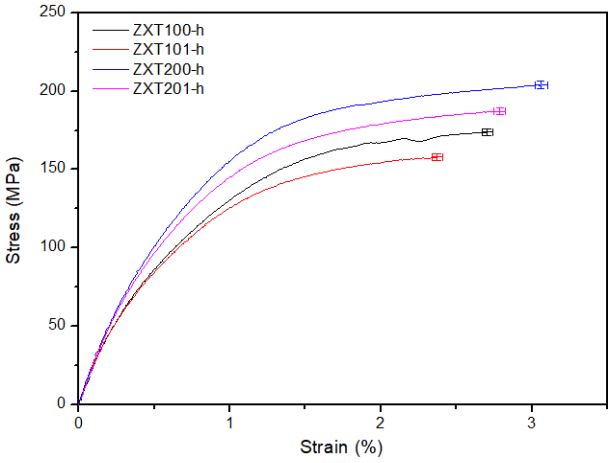

Figure 8. Stress-Strain curve of Sn added alloys after hot rolling (h: Hot rolled).

As it is seen from Table 3 and Table 4, 0.5 wt% Sn containing alloys (ZXT100 and ZXT200) have slightly higher yield strength, and much higher strain at fracture than ZX10 and ZX20 alloys (Sn free alloys). However, a small reduction in tensile strength of the alloys was observed. when the Sn ratio of the alloys increased from 0.5 wt% to 1.0 wt% (ZXT101 and ZXT201), yield and tensile strengths of the alloys as well as strain at fracture decrease. Therefore, it can be concluded that small amount of Sn (around 0.5 wt%) is beneficial to improve the yield strength and strain at fracture of the alloy, but increasing Sn ratio has a negative influence on the mechanical properties of the Mg-Ca-Zn alloys.

Hot rolling of Sn containing alloys (ZXT100-h, ZXT200-h, ZXT101-h, and ZXT201-h) results in higher yield strength and tensile strength but much lower strain at fracture than unrolled Sn containing alloys (ZXT100, ZXT200, ZXT101, and ZXT201). Therefore, it can be said that the strength of the Sn containing alloys can be improved by using thermomechanical processes such as hot rolling at the expense of ductility. As the Sn ratio of the alloys is taken into consideration, it is seen that the mechanical properties of the hot rolled alloys containing higher Sn have lower yield strength, tensile strength, and strain at fracture too. On the other hand, increasing the Zn ratio at constant Sn ratio has beneficial effects on the strengths and strain values of the alloys before and after hot rolling. The increase in yield strength, tensile strength, and decrease in strain of the hot rolled alloys can be mainly attributed to the formation of fine grain structures during the dynamic recrystallization (DRX) process and the distribution of finer secondary phases that improve the strength of the alloys by the Zenner pinning mechanism.

As a summary, a comparison of the yield strength and tensile strength of the alloys shows that Zn is more effective than Sn to improve the strengths of the alloys. In addition, the strength of the alloys can be further improved with the application of a thermomechanical process. Among the alloys studied here, it is determined that ZX20-h alloy has the highest yield strength and tensile strength (177.44 MPa and 240.50 MPa, respectively) and a moderate strain value (5.28). It is known that the yield and tensile strengths of a cortical bone are in the range of 105 MPa to 114 MPa and 35 MPa to 283 MPa, respectively [18,33-35]. Therefore, the obtained results seem mechanically sufficient to be used as a bone support plate. Zhao *et al.* In their study, they determined the yield strength and tensile strength results of Mg-1Zn and Mg-1Zn-0.5Sn alloys as 110 MPa to 115 MPa and 211 MPa to 239 MPa, respectively [18]. The literature results on the mechanical characteristics of Mg-based alloys confirm the results obtained here.

3.6 Corrosion test results

Corrosion samples in a rectangular prism shape with an equal surface area were used in immersion corrosion tests. Immersion corrosion rates of the alloys were determined using Equality.1 (Equation (1)) [36]. Weight loss methods are essential in corrosion studies because they provide a quantitative measure of material degradation over time, helping assess the corrosion rate and extent [37]. Oxidation reactions of a metal in a corrosive solution are given in Equation (2-5) [38]. In general, the corrosion process involves a series of electrochemical reactions. In these electrochemical reactions, oxide, hydroxide, and H_2 gas are formed during corrosion. The chemical reactions observed in biodegradable metal alloys, including magnesium and its alloys, are shown by the following four equations, and these reactions express the corrosion process [28].

$$CPR = (K.W)/(d.A.t) \quad (1)$$

(W: weight loss (mg), d: density ($g \cdot cm^{-3}$), A: surface area (cm^2), t: time (h), K: constant (87,6 for $mm \cdot year^{-1}$))

$$M \rightarrow Mn^{+} + ne^{-} \text{ (Anodic reaction)} \quad (2)$$
$$nH_2O + ne^{-} \rightarrow nH_2 + nOH^{-} \text{ (Cathodic reaction)} \quad (3)$$
$$Mn^{+} + nOH^{-} \rightarrow M(OH)n \text{ (Protective layer)} \quad (4)$$
$$M(s) + nH_2O \rightarrow M(OH)n + nH_2 \text{ (Total reaction)} \quad (5)$$

Metal materials can be protected from corrosion to some extent by the protective oxide layer formed on their surfaces. Therefore,

the corrosion resistance of metal materials depends on the continuity and protective properties of the oxide layer. When biodegradable metal materials come into contact with body fluids in the body, they are exposed to the effects of amino acids, proteins, lipids, various salts, and other organic compounds [38]. As a result, electrochemical reaction given in Equation (2-4) takes place. During corrosion, a corrosion product layer forms on the metal surface (Equation (4)). However, since the fluid environment in the body contains a very high amount of Cl^- ions, it will cause the M(OH)n protective layer to break down. It also causes pitting type corrosion on the metal surface [38]. As the corrosion process continues, calcium phosphate-based apatites precipitate on the undissolved M(OH)n layer. The main reason for this is shown as localized alkalization of the physiological environment and sufficient saturation with calcium phosphate [38].

The calculated immersion corrosion rates are given in Table 5.

The weight loss of the alloys measured using a 1/10000 sensitive balance showed that the weight loss of the alloys decreased with immersion time. As a result, the immersion corrosion rate of the alloys showed declining behavior with increasing immersion time, as it is seen in Table 5. The decrease in corrosion rate with immersion time is due to the formation and growth of a corrosion product layer that slows down oxygen penetration and prevents further oxidation reactions. When the corrosion rates of unrolled alloys are compared, it is found that increasing the Zn ratio of the alloys with and without Sn reduces the corrosion rate. However, Sn addition up to 0.5 wt% improves the corrosion resistance of the alloy. However, the addition of Sn greater than 0.5 wt% has a negative effect on the corrosion resistance of the alloy. The increased corrosion rate of the high Zn and Sn containing alloy (ZX201) can be attributed to the higher volume fraction of the secondary phases that cause the formation of more galvanic coupling sites. Similarly, Moussa *et al.* determined that the corrosion rates of cast Mg-Ca-Zn alloys were higher than the alloys produced by other production methods in their studies. It was explained by the larger $Ca_2Mg_6Zn_3$ particles, which serve as micro-galvanic cathodes, increasing the corrosion rate of the alloys [39].

Immersion corrosion results of hot rolled alloys showed that hot rolling results in higher corrosion rates. The higher corrosion rates of alloys after hot rolling can be explained by the formation of micro-cracks, increased defect density, residual stresses, texture, and the presence of coarse and fine grains due to incomplete recrystallization, which also increases the galvanic corrosion. There are two contrasting perspectives on how grain size impacts the corrosion characteristics of Mg alloys. Several studies have shown that the presence of grain boundaries may enhance corrosion resistance by reducing the size of the galvanic cell [40-42]. Others argue that the grain boundary acts as a crystallographic defect, increasing the rate of corrosion [40,43,44]. Since the electrode potential of grain boundaries is higher than that of the matrix, more contaminants and solute atoms accumulate along the grain boundaries. Consequently, more galvanic corrosion sides that form in close proximity to the grain boundary accelerate corrosion [40]. Similar to these studies, ours clearly show that corrosion rates are high in ZX alloys and hot rolled alloys. Among the alloys, ZXT200 showed the lowest corrosion rate 5.10 $mm \cdot year^{-1}$ after 10 day of immersion. It was followed by the ZXT100 alloy with its 6.75 $mm \cdot year^{-1}$ corrosion rate after 10 day of immersion. However, ZX20-h, with the highest mechanical properties among the alloys has 13.56 $mm \cdot year^{-1}$ corrosion rate after 10 day of immersion.

3.7 Microscopic analyses after corrosion

images of the alloys after 10 day of immersion corrosion tests are shown in Figure 9.

It is seen that the degradations of ZX10-h (Figure 9(g)), ZXT100-h (Figure 9(i)), and ZXT101-h (Figure 9(j)) are much higher than those of other alloys. Therefore, ZX10-h, ZXT100-h, and ZXT101-h alloys are expected to have higher corrosion rates than the others. The corrosion rates (10 day immersion) given in Table 5 show that ZX10-h, ZXT100-h, and ZXT101-h alloys have very high corrosion rates.

Scanning Electron Microscope (SEM) surface images of ZX20 and ZXT201 alloys after 1 day corrosion were given in Figure 10(a-b), and the areas marked with red squares in these figures are shown in Figure 10(c-d) at higher magnification.

When Figure 10 is examined, it is seen that surface oxidations and pitting corrosion occurred during the immersion corrosion tests. It is known that impurities, alloying elements, microstructure, secondary phases, etc. affect the corrosion rates of alloys. It is considered that the presence of porosities in cast alloys plays an important role in the formation of pitting type corrosion. Micro galvanic corrosion occurs at the interface between the Mg matrix and the $Ca_2Mg_6Zn_3$

Table 5. Corrosion rate of alloys (h: Hot rolled).

Designation	Corrosion rate (CRP) ($mm \cdot year^{-1}$)		
	1 day	5 day	10 day
ZX10	28.22	15.69	11.50
ZX20	15.39	10.19	7.50
ZXT100	16.15	9.76	6.75
ZXT101	11.16	8.76	7.53
ZXT200	9.39	8.45	5.10
ZXT201	10.27	11.35	7.15
ZX10-h	190.39	50.42	31.98
ZX20-h	11.63	15.10	13.56
ZXT100-h	89.83	51.38	33.60
ZXT101-h	51.95	33.53	26.89
ZXT200-h	16.45	15.76	10.13
ZXT201-h	11.71	17.79	10.29

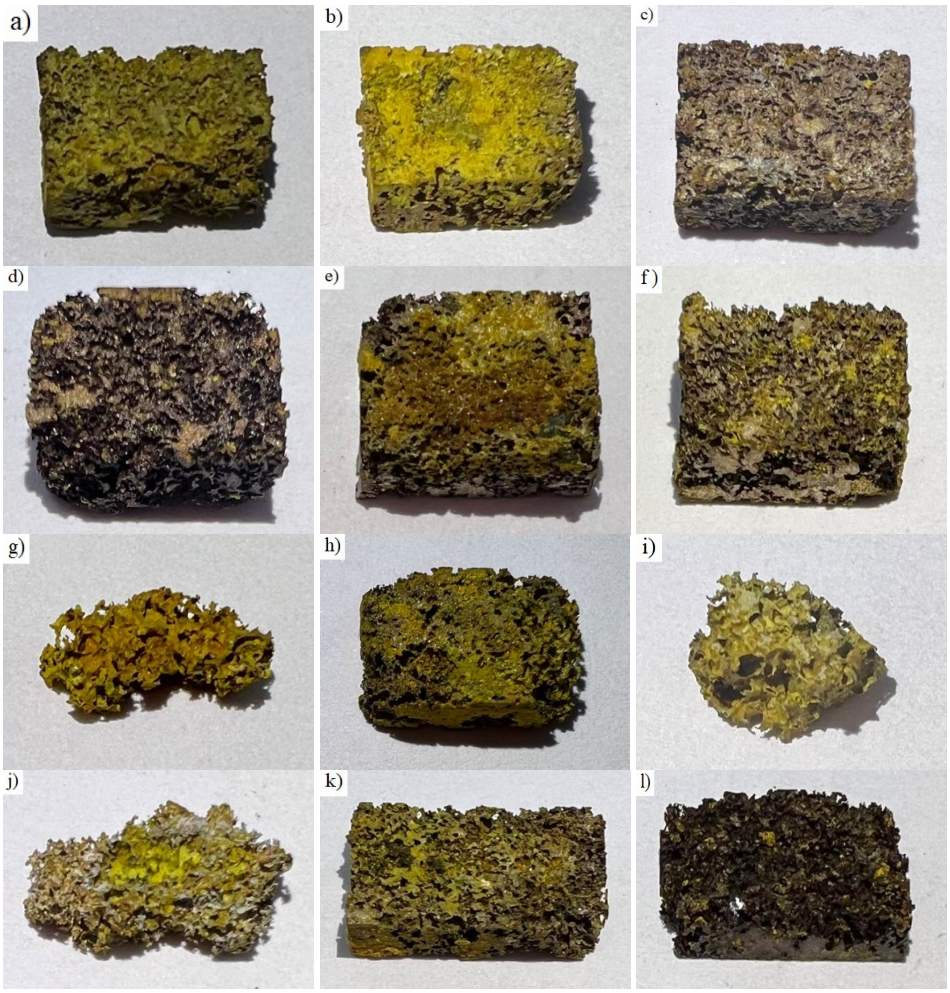

Figure 9. Macro images of all alloys after 10 day of corrosion: (a) ZX10, (b) ZX20, (c) ZXT100, (d) ZXT101, (e) ZXT200, (f) ZXT201, (g) ZX10-h, (h) ZX20-h, (i) ZXT100-h, and (j) ZXT101-h, k).

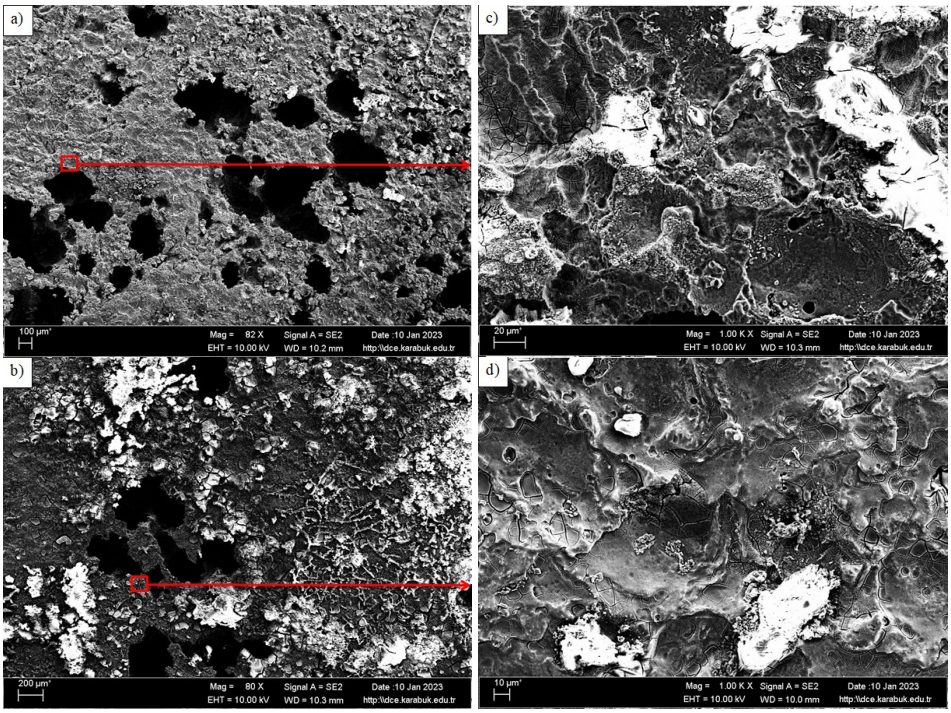

Figure 10. Scanning electron microscope images after corrosion: (a) ZX20-c, (b) ZXT201-c, for macro size, and (c-d) enlarged images of the marked areas in a-b. (c: Corrosion).

secondary phase. As a result, microcracks form between the galvanic couples. As the corrosion progresses, the magnesium matrix around the $Ca_2Mg_6Zn_3$ secondary phase continuously dissolves, separation between the Mg matrix and $Ca_2Mg_6Zn_3$ phase occurs, and eventually, the $Ca_2Mg_6Zn_3$ phase fells out of the experimental samples and leaves a cavity on the sample surface. Additionally, the presence of corrosion pits that increase the contact area between the simulated body fluid (SBF) and the Mg matrix causes a higher corrosion rate [32].

3.8 Tensile properties after immersion corrosion

In order to evaluate the strength of the alloys after corrosion, tensile tests were applied to the samples immersed in a 1 day corrosive medium because some of the samples, severely corroded after 5 day and 10 day immersions, were not suitable for tensile tests. The tensile characteristics of the alloys without Sn after a 1 day immersion corrosion test are shown in Table 6 and Figure 11, while the tensile properties of Sn containing alloys after 1 day corrosion tests are shown in Table 7 and Figure 12 and Figure 13.

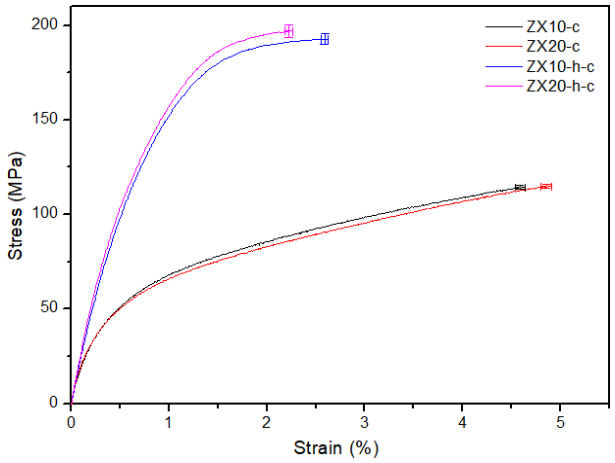

Figure 11. Stress-Strain curve of alloys without Sn addition after immersion corrosion for 1 day (c: Corrosion, h-c: Hot rolled before corrosion).

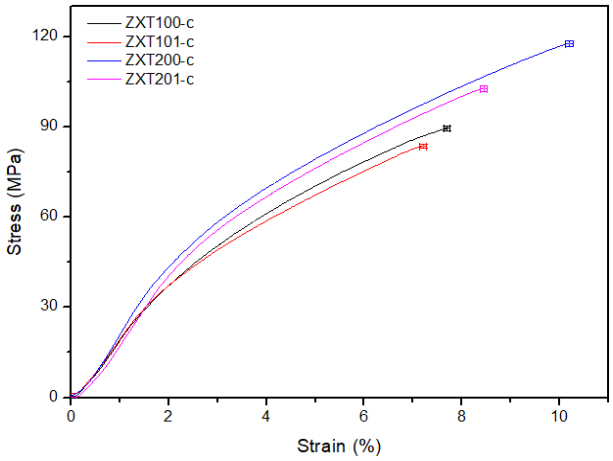

Figure 12. Strain-Stress curve of non-hot rolled Sn added alloys after 1 day of corrosion (c: Corrosion).

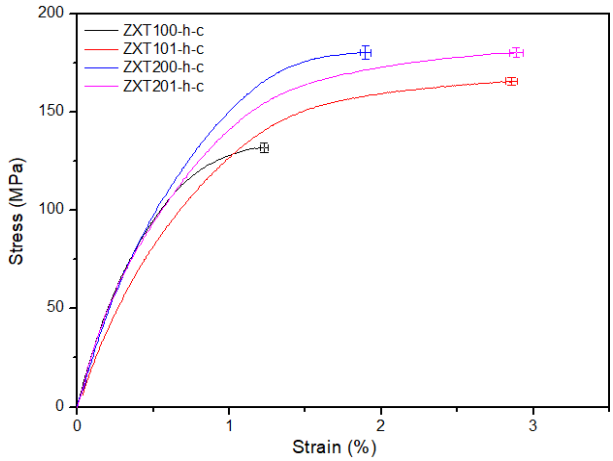

Figure 13. Strain-Stress curve of hot rolled Sn added alloys after 1 day of corrosion (c: Corrosion, h-c: Hot rolled before corrosion).

Table 6. Tensile characteristics of alloys without Sn addition after immersion corrosion for 1 day (c: Corrosion, h-c: Hot rolled before corrosion).

Alloys	Yield strength (σ_y) (MPa)	Tensile strength (σ) (MPa)	Strain (ε) ($mm \cdot mm^{-1}$)
ZX10-c	45.69	114.47 ± 0.91	4.60 ± 0.05
ZX20-c	47.56	114.84 ± 0.88	4.86 ± 0.05
ZX10-h-c	123.84	192.74 ± 2.66	2.59 ± 0.04
ZX20-h-c	124.78	197.00 ± 3.32	2.45 ± 0.04

Table 7. Tensile properties of Sn added alloys after immersion corrosion for 1 day (c: Corrosion, h-c: Hot rolled before corrosion).

Alloys	Yield strength (σ_y) (MPa)	Tensile strength (σ) (MPa)	Strain (ε) ($mm \cdot mm^{-1}$)
ZXT100-c	47.63	92.58 ± 0.78	7.76 ± 0.07
ZXT101-c	35.28	84.54 ± 0.77	7.66 ± 0.07
ZXT200-c	49.54	118.66 ± 0.95	10.44 ± 0.08
ZXT201-c	44.19	103.69 ± 0.91	8.92 ± 0.07
ZXT100-h-c	99.66	132.00 ± 2.49	1.33 ± 0.02
ZXT101-h-c	104.50	165.84 ± 1.94	2.86 ± 0.04
ZXT200-h-c	119.98	180.50 ± 3.40	2.09 ± 0.04
ZXT201-h-c	102.80	180.30 ± 2.51	3.16 ± 0.04

The stress-strain curves of the alloys after corrosion indicate that ductile fracture occurred in the alloy. In addition, tensile test results after 1 day corrosion show that a drop in yield strength and tensile strength before and after hot rolling occurred due to the negative effects of the corrosion on the chemical stability and structure of the alloys. Moreover, when the mechanical properties of the corroded alloys with and without hot rolling were compared, it was observed that the yield and tensile strengths of the hot rolled alloys are much higher than those of the unrolled alloys after immersion corrosion. Tensile test results of the alloys after corrosion also showed similar results as before corrosion such that Zn has positive impact while more than 0.5 wt% Sn containing alloys have lower mechanical properties. Among the alloys, ZX20-h-c alloy exhibited the highest yield and tensile strengths, (124.68 MPa and 197.00 MPa, respectively) after immersion corrosion. In addition, it is seen that alloys with high Zn content have better mechanical properties. It is considered that preferential degradation of secondary phases, formation of large and connected porosities, degradation of grain boundaries, and chemical weakening of the alloys are responsible for the reduction in mechanical properties after immersion corrosion tests.

4. Conclusions

In this study, research was conducted on six distinct Mg-Zn-Ca/Sn alloys. After the castings, the alloys underwent homogenization heat treatment, and hot rolling. The following outcomes were achieved:

- Hot rolling results in a finer grain size and better mechanical properties.
- Zn improves the mechanical properties of the Mg-Zn-Ca alloys.
- Small amount of Sn (around 0.5%) is beneficial to improve the mechanical properties. Increasing Sn ratio results in lower mechanical properties.
- Corrosion rate of the alloys decreases with increasing Zn ratio.
- Sn addition up to 0.5 wt% improves the corrosion resistance of the alloy. However, more than 0.5 wt% Sn has negative impact on the corrosion resistance of the alloy.
- Hot rolling has negative effect on the corrosion resistance of the alloys.

Acknowledgment

This study was supported by the Scientific Research Projects Coordination Unit of Karabuk University. Project Number: KBUBAP-21-DR-011.

References

[1] V. Tsakiris, C. Tardei, and F. M. Clicinschi, "Biodegradable Mg alloys for orthopedic implants–A review," *Journal of Magnesium and Alloys*, vol. 9, no. 6, pp. 1884-1905, 2021.

[2] S. Kamrani, and C. Fleck, "Biodegradable magnesium alloys as temporary orthopaedic implants: a review," *Biometals*, vol. 32, pp. 185-193, 2019.

[3] C. Lhotka, T. Szekeres, I. Steffan, K. Zhuber, and K. Zweymüller, "Four-year study of cobalt and chromium blood levels in patients managed with two different metal-nonmetal total hip replacements," *Journal of Orthopaedic Research*, vol. 21, no. 2, pp. 189-95, 2003.

[4] J. J. Jacobs, N. J. Hallab, A. K. Skipor, and R. M. Urban, "Metal degradation products: a cause for concern in metal-metal bearings," *Clinical Orthopaedics and Related Research*, vol. 417, pp. 139-147, 2003.

[5] J. A. Bishop, A. A. Palanca, M. J. Bellino, and D. W. Lowenberg, "Assessment of compromised fracture healing," *Journal of the American Academy of Orthopaedic Surgeons*, vol. 20, no. 5, pp. 273-282, 2012.

[6] O. Bostman, J. Viljanen, S. Salminen, and H. Pihlajamäki, "Response of articular cartilage and subchondral bone to internal fixation devices made of poly-L-lactide: a histomorphometric and microradiographic study on rabbits," *Biomaterials*, vol. 21, pp. 2553-2560, 2000.

[7] J. Nagels, M. Stokdijk, and P. M. Rozing, "Stress shielding and bone resorption in shoulder arthroplasty," *Journal of Shoulder and Elbow Surgery*, vol. 12, pp. 35-39, 2003.

[8] H. S. Han, S. Loffredo, I. Jun, J. Edwards, Y-C. Kim, H-K. Seok, F. Witte, D. Mantovani, and S. Glyn-Jones, "Current status and outlook on the clinical translation of biodegradable metals," *Materials Today*, vol. 23, pp. 57-71, 2019.

[9] D. Zhao, F. Witte, F. Lu, J. Wang, J. Li, and L. Qin, "Current status on clinical applications of magnesium-based orthopaedic implants: A review from clinical translational perspective," *Biomaterials,* vol. 112, pp. 287-302, 2017.

[10] D. Persaud-Sharma, and A. Mcgoron, "Biodegradable magnesium alloys: Areview of material development and applications," *Journal of Biomimetics, Biomaterials and Biomedical Engineering,* vol. 12, pp. 25-39, 2011.

[11] L. Zheng, H. Nie, W. Liang, H. Wang, and Y. Wang, "Effect of pre-homogenizing treatment on microstructure and mechanical properties of hot-rolled AZ91 magnesium alloys," *Journal of Magnesium and Alloys*, vol. 4, no. 2, pp. 115-122, 2016.

[12] X. N. Gu, and Y. F. Zheng, "A review on magnesium alloys as biodegradable materials," *Frontiers of Materials Science*, vol. 4, pp. 111-115, 2010.

[13] M. M. Avedesian, and H. Baker, ASM Specialty Handbook: Magnesium and Magnesium Alloys. United State of America: ASM international, 1999.

[14] L. Hou, Z. Li, Y. Pan, L. Du, X. Li, Y. Zheng, and I. Ii, "In vitro and in vivo studies on biodegradable magnesium alloy," *Progress in Natural Science: Materials International*, vol. 24, no. 5, pp. 466-471, 2014.

[15] D. P. Sharma, and A. Mcgoron, "Biodegradable magnesium alloys: a review of material development and applications," *Journal of Biomimetics, Biomaterials and Tissue Engineering*, vol. 12, pp. 25-39, 2012.

[16] T. Kraus, S. F. Fischerauer, A. C. Hanzi, P. J. Uggowitzer, J. F. Löffler, and A. M. Weinberg, "Magnesium alloys for temporary implants in osteosynthesis: in vivo studies of their degradation and interaction with bone," *Acta Biomaterialia*, vol. 8, no, 3, pp. 1230-1238, 2012.

[17] C. Zhao, F. Pan, S. Zhao, H. Pan, K. Song, and A. Tang, "Microstructure, corrosion behavior and cytotoxicity of biodegradable Mg–Sn implant alloys prepared by sub-rapid

solidification," *Materials Science and Engineering: C*, vol. 54, pp. 245-251, 2015.

[18] W. Zhao, J. Wang, J. Weiyang, B. Qiao, Y. Wang, Y. Li, and D. Jiang, "A novel biodegradable Mg-1Zn-0.5 Sn alloy: Mechanical properties, corrosion behavior, biocompatibility, and antibacterial activity," *Journal of Magnesium and Alloys*, vol. 8, no. 2, pp. 374-386, 2020.

[19] W. Jiang, and W. Yu "In vitro degradation behavior, mechanical properties, and cytocompatibility of biodegradable Mg-1Zn-XSn alloys," *Crystals*, vol. 12, p. 1219, 2022.

[20] W. Jiang, J. Wang, W. Zhao, Q. Liu, D. Jiang, and S. Guo, "Effect of Sn addition on the mechanical properties and bio-corrosion behavior of cytocompatible Mg–4Zn based alloys," *Journal of Magnesium and Alloys*, vol. 7, np. 1, pp. 15-26, 2019.

[21] N. El-Mahallawy, H. Palkowski, H. G. Breitinger, A. Klingner, M. Shoeib, and A. Diaa, "Microstructure, mechanical properties, cytotoxicity, and bio-corrosion of micro-alloyed Mg–x Sn–0.04 Mn alloys for biodegradable orthopedic applications: Effect of processing techniques," *Journal of Materials Research,* vol. 36, pp. 1456-1474, 2021.

[22] E. Zhang, and L. Yang, "Microstructure, mechanical properties and bio-corrosion properties of Mg–Zn–Mn–Ca alloy for biomedical application," *Materials Science and Engineering: A*, vol. 497, pp. 111-118, 2008.

[23] S. A. Wahid, Y. G. Jung, S. Ha, and H. K. Lim, "Effect of CaMgSn ternary phase on the aging response of Mg-Sn-Zn-Ca alloys," *Journal of Korea Foundry Society*, vol. 8, pp. 75-81, 2018.

[24] P. K. Rout, S. Roy, and D. Rathore, "Recent advances in the development of Mg-Ca-Zn alloys as biodegradable orthopedic implants," *Materials Today: Proceedings*, 2023.

[25] H. Li, D. Liu, Y. Zhao, F. Jin, and M. Chen, "The influence of Zn content on the corrosion and wear performance of Mg-Zn-Ca alloy in simulated body fluid," *Journal of Materials Engineering and Performance*, vol. 25, pp. 3890-3895, 2016.

[26] H. Du, Z. Wei, X. Liu, and E. Zhang, "Effects of Zn on the microstructure, mechanical property and bio-corrosion property of Mg–3Ca alloys for biomedical application," *Materials Chemistry and Physics*, vol. 125, pp. 568-575, 2011.

[27] H. R. Bakhsheshi-Rad, M. R. Abdul-Kadir, M. H. Idris, and S. Farahany, "Relationship between the corrosion behavior and the thermal characteristics and microstructure of Mg–0.5Ca–xZn alloys," *Corrosion Science*, vol. 64, pp. 184-197, 2012.

[28] X. Gu, Y. Zheng, Y. Cheng, S. Zhong, and T. Xi, "In vitro corrosion and biocompatibility of binary magnesium alloys," *Biomaterials*, vol. 30, no. 4, pp. 484-498, 2009.

[29] A. Incesu, "Design and production of biodegradable Mg-Zn-Ca VE Mg-Zn-Ca-Mn magnesium alloys for biomedical applications," Ph.D. dissertation, Department of Metallurgical and Materials Engineering, Karabuk University, Karabuk, Turkey, 2019.

[30] ASM International Handbook Committee, "ASM Metals Handbook Volume 8 Metallography, Structures and Phase Diagrams," 8th ed. ASM International, USA: 1990.

[31] L. Lu, A. K. Dahle, J. A. Taylor, and D. H. StJohn, "Theoretical and practical considerations of grain refinement of Mg-Al alloys," *Materials Science Forum*, vol. 488-489, pp. 299-302, 2005.

[32] L. Wei, J. Li, Y. Zhang, and H. Lai, "Effects of Zn content on microstructure, mechanical and degradation behaviors of Mg-xZn-0.2 Ca-0.1 Mn alloys," *Materials Chemistry and Physics*, vol. 241, p. 122441, 2020.

[33] D. Hong, D-T. Chou, B. Lee, B. Collins, Z. Tan, Z. Dong, and P. N. Kumta,"In vitro degradation and cytotoxicity response of Mg–4% Zn–0.5% Zr (ZK40) alloy as a potential biodegradable material," *Acta biomaterialia*, vol. 9, no. 10, pp. 8534-8547, 2013.

[34] X. Zhang, G. Yuan, L. Mao, J. Niu, and W. Ding, "Biocorrosion properties of as-extruded Mg–Nd–Zn–Zr alloy compared with commercial AZ31 and WE43 alloys," *Materials Letters*, vol. 66, no. 1, pp. 209-211, 2012.

[35] F. Witte, N. Hort, C. Vogt, S. Cohen, K. U. Kainer, R. Willumeit, and F. Feyerabend, "Degradable biomaterials based on magnesium corrosion," *Current opinion in solid state and materials science,* vol. 12, no. 5-6, pp. 63-72, 2008.

[36] M. O. Nwankwo, P. A. Nwobasi, P. O. Offor, and N. E. Idenyi "Unification of the quadratic model equations of the inhibition characteristics of acidifield ocimum basilicum on the corrosion behavior of mild steel," *Journal of Minerals and Materials Characterization and Engineering*, vol. 1, pp. 367-373, 2013.

[37] H. M. Lieth, M. A. Jabbar, R. J. Jassim, and R. Al-Sabur "Optimize the corrosion behavior of AISI 204Cu stainless steel in different environments under previous cold working and welding," *Metallurgical Research & Technology*, vol. 120, no. 4, pp. 415-424, 2023

[38] H. Gerengi, E. Kaya, and M. Cabrini "Magnesium (99.95%) potential to use as a biodegradable material," *Journal of Advanced Technology Sciences*, vol. 6, no. 2, pp. 10-25, 2017.

[39] M. E. Moussa, M. M. M. Salem, M. A. Hamid, M. H. Gomaa, A. Abd-Elwahed, I. M. Ghayad, and A. A. Mohamed, "Mechanical integrity and in vitro degradation behavior of Mg–Zn–Ca biodegradable alloy prepared by different casting technologies," *International Journal of Metalcasting*, pp. 1-19, 2023.

[40] L. Yang, Y. Feng, Y. He, L. Yang, H. Liu, X. Wang, C. Peng, and R. Wang, "Effect of Sc/Sm microalloying on microstructural and properties of Mg-2Zn-0.3 Ca biodegradable alloy," *Journal of Alloys and Compounds*, vol. 907, p. 164533, 2022.

[41] G. R. Argade, S. K. Panigrahi, and R. S. Mishra "Effects of grain size on the corrosion resistance of wrought magnesium alloys containing neodymium," *Corrosion Science*, vol. 58, pp. 145-151, 2012.

[42] J. H. Chu, L. B. Tong, Z. H. Jiang, D. N. Zou, Q. J. Wang, S. F. Liu, and H. J. Zhang, "A comparison study of Ce/La and Ca microalloying on the bio-corrosion behaviors of extruded Mg-Zn alloys," *Journal of Magnesium and Alloys*, vol. 8, no. 4, pp. 1269-1280, 2020.

[43] G. L. Song, and Z. Xu "The surface, microstructure and corrosion of magnesium alloy AZ31 sheet," *Electrochimica Acta*, vol. 55, no. 13, pp. 4148-4161, 2010.

[44] Y. Wang, Y. Zhang, and H. Jiang "Effect of grain size uniformity and crystallographic orientation on the corrosion behavior of Mg-2Zn-1Al bar," *Materials Characterization*, vol. 179, p. 111374, 2021.